Chemical Science

EDGE ARTICLE

View Article Online
View Journal | View Issue

Cite this: *Chem. Sci.*, 2018, **9**, 4009

Composition-adjustable Ag–Au substitutional alloy microcages enabling tunable plasmon resonance for ultrasensitive SERS†

Xiaotian Wang,‡[a] Guanshui Ma,‡[a] Anran Li,‡[a] Jian Yu,[a] Zhao Yang,[a] Jie Lin,[a] Ang Li,[b] Xiaodong Han[b] and Lin Guo *[a]

Received 26th February 2018
Accepted 21st March 2018

DOI: 10.1039/c8sc00915e

rsc.li/chemical-science

Engineering the surface plasmon resonance (SPR) properties is a critical issue for improving device performance in the fields of plasmonics, nanophotonics, optoelectronics, and electrochemistry. Here, we demonstrated a programmable manipulation of the surface plasmon resonance (SPR) effect using composition-adjustable Ag–Au substitutional alloy microcages (SAMCs) through a facile $NaBH_4$-cooperative galvanic replacement reaction. The SPR frequency of the Ag–Au SAMCs can be continuously and exquisitely manipulated without resonance damping or broadening *via* accurate adjustment of the elemental composition distribution at the perfect homogeneity on the atomic-level. Significantly, both the tunable SPR frequency and excellent chemical stability synergistically endow the hollow Ag–Au SAMCs with excellent SERS sensitivity and reproducibility, which lays a foundation for the realization of trace detection of thiram at an ultralow concentration of 1×10^{-12} M. This strategy is a promising candidate for efficient promotion of the SERS activity for metal-based substrates.

Introduction

Tunable manipulation of surface plasmon resonance (SPR) properties is a critical issue for boosting the performance of plasmonic materials and devices in the fields of photocatalysis,[1–3] optical waveguides,[4] surface-enhanced Raman scattering (SERS),[5–11] and photovoltaic cells.[12] For example, in order to ensure the signal-to-noise ratio is high enough, the excitation wavelength should be properly changed to avoid the fluorescence of probe molecules in SERS detection. If the SPR frequency of the SERS substrate can be easily tuned to match well with the change of incident wavelength, a programmable SERS technology can be realized. Typically, the peak position of SPR can be shifted by changing the geometry of plasmonic structures, *i.e.* the size and shape. However, the corresponding change of dipole moment accompanied with the change of geometry would result in undesirable spectral broadening and resonance damping.[13–16] Also, introducing a dielectric medium to change the dielectric constant of the surroundings can modulate the plasmon oscillation strength and frequency,[17] but this would contaminate the surface of plasmonic structures and finally result in the performance deterioration of devices, such as decreased sensitivity of SERS sensors.[18–21] Fortunately, alloying noble-metal nanoparticles might be a promising strategy as it could not only effectively modulate the dielectric function, but also avoid the geometry effect and the surface contamination.[22–25] Although some achievements have been made in the component regulation of the Ag–Au alloy nanoparticles,[26–29] it is difficult to achieve compositional homogeneity of Ag and Au across a 3D complex alloy nano/micro-structure. Nano/microstructured Ag–Au alloy can be produced from galvanic replacement of an Ag nanoparticle with a salt of Au,[30–33] resulting from a more positive potential of Au^{3+}/Au than that of Ag^{+}/Ag. A conventional approach is using $HAuCl_4$ solution to carry out the galvanic replacement reaction (GRR) *via* heating to enhance the inter-diffusion between Ag and Au.[26–33] However, the fast reaction rate and the lack of control over the ratio and the distribution of the Ag and Au components may cause bimetallic nanodomains in the alloy nano/micro-structures.[30,31] Inhomogeneous composition distribution would unavoidably cause serious bimetallic plasmon coupling, which will result in undesirable spectral broadening and resonance damping.[34] Therefore, developing a novel strategy to synthesize composition-adjustable alloy nano/micro-structures with uniform composition distribution is an urgent issue.

In this work, we demonstrated novel composition-tunable Ag–Au substitutional alloy microcages (SAMCs) with homogeneous element distribution on the atomic-level *via* a facile $NaBH_4$-cooperative GRR strategy. During the alloying reaction,

[a]*School of Chemistry, Key Laboratory of Bio-Inspired Smart Interfacial Science and Technology, Ministry of Education, Beijing Advanced Innovation Center for Biomedical Engineering, Beihang University, Beijing, P. R. China. E-mail: guolin@buaa.edu.cn*

[b]*Beijing Key Lab of Microstructure and Property of Advanced Materials, Beijing University of Technology, Beijing 100024, P. R. China*

† Electronic supplementary information (ESI) available. See DOI: 10.1039/c8sc00915e

‡ These authors contributed equally to this work.

the $NaBH_4$ was used to promote diffusion of the Ag and Au components rather than the conventional heating approach, making the co-reduction process of Ag and Au more moderate and controllable. The hollow porous structure of the Ag–Au SAMCs not only serves as an ideal optical resonant cavity to generate strong SPR coupling between the inner and outer surfaces of the microcage, but also endows the Ag–Au SAMCs with abundant "hot-spots" for generating a strong local electromagnetic field (LEMF). Moreover, we found that the SPR frequency of the Ag–Au SAMCs can be continuously manipulated with no further resonance damping or broadening when adjusting the percentage of Au atoms in the range 0–23%. Typically, by adjusting the percentage of Au atoms to 14.2%, the SPR frequency of the Ag–Au SAMCs can be modulated to match well with the excitation wavelength of 633 nm, leading to a remarkable enhancement factor (EF) of up to 1.3×10^{11}, which is the highest value among the reported alloy nano/micro-structures. The ultrahigh sensitivity enables the Ag–Au SAMCs to detect trace amounts of thiram at an ultralow concentration of 1×10^{-12} M. Furthermore, the presence of Au endows the Ag–Au SAMCs with excellent oxidation resistance and chemical stability, providing a promising SERS substrate for trace detection in an oxidative environment.

Results and discussion

Ag and Au were selected as plasmonic components to prepare the composition-adjustable alloy microstructures due to their strong SPR effects in the visible light range and excellent miscibility in any proportion.[35–37] The synthesis procedures of composition-adjustable Ag–Au SAMCs are shown in Scheme 1 (the details are given in sections S1 and S2 in the ESI †). Firstly, the Ag^+ in $AgNO_3$ was reduced to Ag using $NaBH_4$, and then the Ag nanoparticles self-assembled on the surface of Cu_2O due to the crosslinking effect of citrate ions between Ag and Cu_2O, forming the Cu_2O@Ag core–shell structures (Process ①). Secondly, after etching the Cu_2O core with acetic acid, octahedral hollow porous Ag microcages (MCs) were obtained (Process ②).[38] Finally, through a novel $NaBH_4$-cooperative GRR, octahedral hollow porous Ag–Au SAMCs were successfully synthesized (Process ③). Different to conventional GRR, the synergistic co-reduction of Au^{3+} and Ag^+ to obtain Ag–Au SAMCs should be ascribed to the cooperation with $NaBH_4$ in the system. When Au^{3+} ions were spontaneously reduced by Ag atoms to generate Au atoms and Ag^+ ions, the released Ag^+ ions on the surface of the Au atoms were immediately reduced back to Ag atoms by the $NaBH_4$, producing the Ag–Au SAMCs. The characterization of samples in each step is shown in Fig. S3.† Moreover, the stoichiometric quantity in Ag–Au SAMCs can be adjusted by changing the amount of $HAuCl_4$. For example, through adding varied amounts of $HAuCl_4$ solution (5 mM) within the range of 0.1 to 0.6 mL into the reaction system, a series of Ag–Au SAMCs with changeable percentages of Au atoms (labeled as 0.1–0.6) were successfully obtained, as shown in Fig. S4.† Scanning electron microscope (SEM) and energy-dispersive X-ray (EDX) mapping analysis demonstrated that the percentage of Au atoms in these Ag–Au SAMCs can be mediated in the range of 5.6–22.7%, as shown in Table S1.†

It was found that the octahedral Ag–Au SAMCs with excellent uniformity could be high-yield synthesized *via* the $NaBH_4$-cooperative GRR. Typically, Fig. 1a shows the high-uniformity of the as-prepared 0.35 Ag–Au SAMCs. The octahedral Ag–Au SAMCs possess sharp corners and edges, which can be attributed to the successful shape duplication of the Cu_2O templates. The size of the octahedral Ag–Au SAMCs is about 600 nm. The thickness of the microcage is around 20 nm, which was characterized by transmission electron microscopy (TEM) and atomic force microscopy (AFM) characterization (Fig. S5 and S6†). The hollow interior structure can be confirmed by the strong colour contrast between the edges (dark) and the center (gray) in the TEM image (Fig. 1a). The high-resolution TEM (HRTEM) image in Fig. 1b clearly shows that the spacing of adjacent lattice fringes is 0.235 nm, which is very close to the lattice constant of (111) planes of both Ag (0.2358 nm) and Ag (0.2355 nm). The corresponding selected area electron diffraction (SAED) pattern in Fig. 1c demonstrates the good crystallinity of the Ag–Au SAMCs, and the concentric rings can be assigned to the (111), (200), (220), and (311) planes, which is consistent with the X-ray diffraction (XRD) characterization (Fig. S7†). The lattice phase of the Ag–Au microcages did not show a detectable change compared to that of the Ag

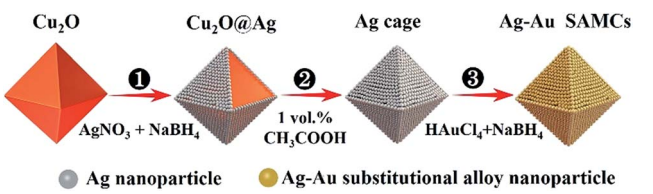

Scheme 1 Schematic illustration of the fabrication strategy for octahedral hollow porous Ag–Au SAMCs through a facile $NaBH_4$-cooperative GRR.

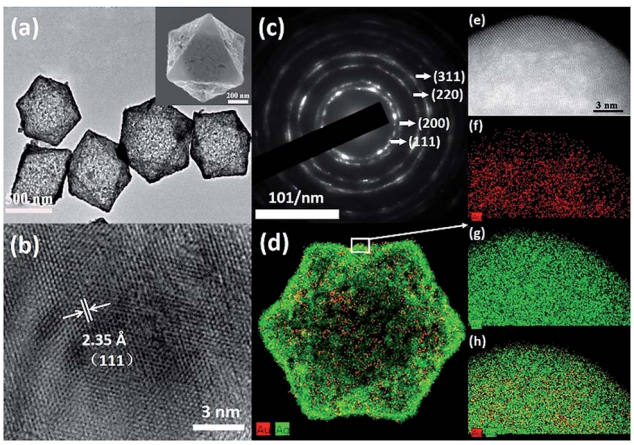

Fig. 1 (a) TEM image, inset: SEM image, (b) HRTEM image, (c) SAED pattern, and (d) HAADF-STEM-EDX elemental mapping of octahedral hollow 0.35 Ag–Au SAMCs. (e) Atomic resolution HAADF-STEM image and (f)–(h) the corresponding elemental maps of Au, Ag and superposition of Ag and Au.

microcages. As the atomic radius of Au is very similar to that of Ag, the substitution of Ag atoms with Au atoms will not result in a change in the Ag lattice constant, which is in favour of the formation of the substitutional alloy. The results of bright-field scanning TEM (BF-STEM) and EDX mapping analysis show that the Ag and Au components distribute uniformly in the Ag–Au SAMCs (Fig. S8†). To further investigate the distribution of the Au and the Ag atoms on the atomic scale, we used aberration-corrected high-angle annular dark-field STEM (HAADF-STEM) and EDX mapping to characterize the Ag–Au SAMCs (Fig. 1d–h). Fig. 1e shows the atomic-resolution HAADF-STEM image of 0.35 Ag–Au SAMCs, in which the atomic columns can be clearly observed. The elemental mappings (Fig. 1f–h) clearly show that the Ag and Au atoms distribute homogeneously on the atomic-level rather than forming individual Ag or Au nanodomains, which provides convincing evidence that the as-synthesized Ag–Au microcages could be regarded as a substitutional alloy of Ag and Au. These results validate the synergistic co-reduction of Au^{3+} and Ag^{+} ions *via* facile $NaBH_4$-cooperative GRR for the formation of Ag–Au SAMCs. Once Ag atoms react with Au^{3+} ions to form Au atoms and Ag^{+} ions, the Ag^{+} ions can be immediately reduced back to Ag atoms by the $NaBH_4$, and then attach to Au atoms to produce a Ag–Au substitutional alloy with homogeneous elemental distribution on the atomic-level. In order to further confirm the critical role of $NaBH_4$ in synthesizing the Ag–Au substitutional alloy, we performed the alloying reaction using only the $HAuCl_4$ solution without $NaBH_4$ as a control experiment. The HAADF-STEM-EDX elemental mapping showed that many Au clusters and nanodomains were formed in the microcage, resulting in the formation of Ag–Au bimetallic MCs (Fig. S9a†). The UV-vis spectra also exhibited undesirable spectral broadening and resonance damping of these Ag–Au bimetallic MCs, which can be attributed to the bimetallic plasmon coupling of the Ag and Au nanodomains (Fig. S9b†).

Although the size of the Ag–Au cages approaches micrometers, the thickness of the cage shell is only 20 nm and thus still has the unique properties of a nanomaterial, such as strong SPR coupling between the inner and outer surface of the cage. Compared with the solid Ag–Au octahedron, the hollow Ag–Au SAMCs exhibit great potential to generate a stronger electric field enhancement, as indicated by the finite-difference time-domain (FDTD) simulations. In a typical simulation, the thickness of the shell for the hollow 0.35 Ag–Au microcage is set to be 20 nm, which is chosen based on the prepared sample. The dielectric functions of Au and Ag were derived from the modified Drude model, considering the 8–9 Lorentzians parts.[39] The dielectric function of the 0.35 Ag–Au alloy was calculated based on the composition-weighted average of Au and Ag,[34] where the Ag–Au alloy is thought to be made up of 14% Au and 86% Ag according to the SEM-EDX mapping analysis (Table S1†). The simulation details are shown in section S10 in the ESI .† Because non-polarized incident light is used in our experiments, the electric field distributions of the octahedral microstructures under incidence with different polarization directions $(\vec{E}_1, \vec{E}_2)$ (which are perpendicular to each other) are calculated to evaluate the average effect of non-polarized incidence on the plasmon resonance and coupling of hollow the Ag–Au SAMCs and its counterpart solid structure. Fig. 2 shows the calculated electric field distributions $(|E|^2/|E_0|^2)$ for the solid Ag–Au octahedron and the hollow Ag–Au SAMC. The orientation of the octahedral microstructures in the simulations is consistent with the orientation of an octahedron laid on the substrate in an experiment, as shown in the inset image in Fig. 1a. The propagating direction of the incident light is perpendicular to the sample surface. The calculated electric-field intensity $(|E|^2/|E_0|^2)$ indicated that the enhanced electric fields were mostly located at the sharp corners or edges for the solid octahedron, while the electric field enhancement at other places was negligible. In contrast, in addition to the strong electric field enhancement at corners or edges, the hollow microcage structure also exhibited strong electric field enhancement at both the inner and outer surface of the shell, which can be attributed to the strong SPR coupling between the inner and outer surfaces of the microcage. The stronger SPR coupling and larger area of electric field enhancement gives the hollow microcage structure more excellent SERS performance than the solid structure.

These composition-adjustable Ag–Au SAMCs provide us with a promising platform to develop tunable plasmon resonance for programmable SERS technology. UV-vis spectroscopy was performed to characterize the SPR properties of these Ag–Au SAMCs, as shown in Fig. 3a. It can be seen that only one sharp resonance band is visible for the Ag–Au SAMCs with different gold content, which suggests that no strong bimetallic plasmon coupling between Au and Ag appears in the system. It is noted that there is also one small peak at the lower wavelength, which can be attributed to the higher order resonance mode of the Ag–Au SAMCs.[40,41] Significantly, the SPR frequency can be continuously red-shifted from 472 to 670 nm with no further SPR

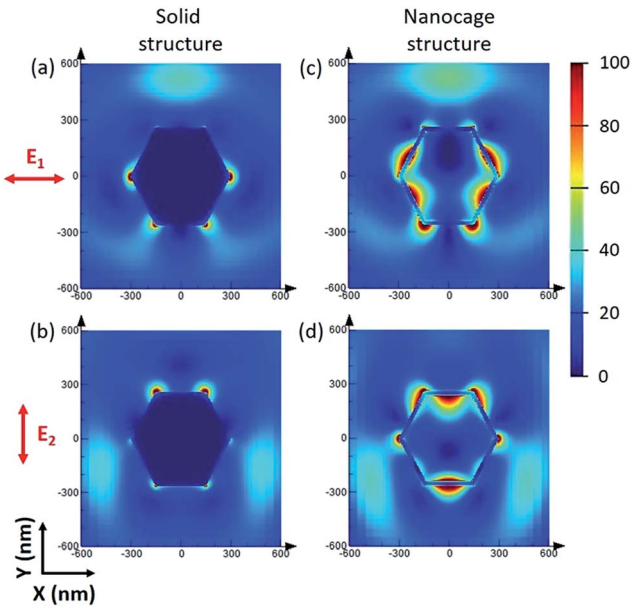

Fig. 2 Calculated electric field distributions $(|E|^2/|E_0|^2)$ for (a) and (b) the solid Ag–Au octahedron and (c) and (d) the hollow Ag–Au SAMCs. The red arrows in the figure show the polarization directions of the incident light.

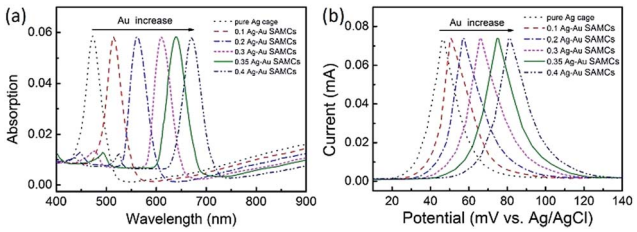

Fig. 3 (a) UV-vis spectra and (b) LSV curves of the as-synthesized Ag–Au SAMCs with different Au content. LSV measurements: 1 M KCl electrolyte, scan rate of 5 mV s^{-1}.

damping or band broadening when increasing the concentration of gold, which might be attributed to the homogeneous elemental distribution in the Ag–Au SAMCs. For the alloy structure, the SPR band is determined by the effective dielectric function of Au–Ag ionic background.[22,23] Based on Mie's theory,[42] the effective dielectric function ($\varepsilon[x, \omega_{IB}(x)]$) in an alloy can be approximately evaluated by the stoichiometric quantities of Au and Ag:[22,34]

$$\varepsilon[x, \omega_{IB}(x)] = x\varepsilon_{Au}[x, \omega_{IB}(Au)] + (1 - x)\varepsilon_{Ag}[x, \omega_{IB}(Ag)] \quad (1)$$

where x is the stoichiometric ratio in the alloy; $\hbar\omega_{IB}(Au) = 1.9$ eV and $\hbar\omega_{IB}(Ag) = 3.9$ eV are the interband transition thresholds of gold and silver, respectively.[34] Based on eqn (1), for the inhomogeneous system of bimetallic mixtures consisting of stacked gold and silver nanodomains, the interband transition threshold ($\omega_{IB}(x)$) is independent of the stoichiometric ratio, that is $\omega_{IB}(x) = \omega_{IB}(Au)$.[23] A small value of $\omega_{IB}(x)$ will lead to the spectral overlap of SPR with the interband transitions, resulting in damping, broadening, and an asymmetric SPR band.[43] In contrast, for the homogeneous system of the substitutional alloy, the interband threshold $\omega_{IB}(x)$ will follow a quasi-linear dependence between $\omega_{IB}(Au)$ and $\omega_{IB}(Ag)$, that is $\omega_{IB}(x) = x\omega_{IB}(Au) + (1 - x)\omega_{IB}(Ag)$.[23] The higher interband threshold $\omega_{IB}(x)$ can effectively avoid the spectral overlap of SPR with the interband transitions, resulting in a quite sharp and symmetric SPR band. Therefore, during the adjustment of the percentage of Au atoms in the range of 0–23%, continuous manipulation of the plasmon resonance of the as-synthesized Ag–Au microcages with no further resonance damping or broadening could be attributed to the perfect homogeneity of the elemental distribution on the atomic-level. This indicates that no bimetallic plasmon coupling occurs within the system, and thus the as-synthesized Ag–Au microcages should be a substitutional alloy rather than a bimetallic complex. However, when the percentage of Au atoms exceeds 25%, it would generate the Au nanodomains, and even Au clusters in partial areas, which will result in the Ag–Au bimetallic complex. Therefore, to avoid bimetallic plasmon coupling and maintain the sharp resonance band, the percentage of Au atoms should not exceed 25% in our experiments.

In addition, it is anticipated that these Ag–Au SAMCs possess better chemical stability due to the introduction of Au, which possesses strong chemical inertia. In order to evaluate the oxidation resistance of these Ag–Au SAMCs, we used linear sweep voltammetry (LSV) to monitor the oxidation potential when increasing the percentage of Au atoms as shown in Fig. 3b. The results clearly showed that the oxidation peak shifted to more positive values from 46.5 to 82.7 mV during the increase of the Au concentration. The significant positive-shift of the oxidation peak of the Ag–Au SAMCs suggests a decrease in work function when increasing the Au composition.[43] The decreased work function can be attributed to the induced electron transfer process from the Ag atom to the Au atom owing to the spontaneous equilibrium of the Fermi level in the alloy structure, resulting in improved oxidation resistance.

To employ the tunable plasmon resonance for developing programmable SERS technology, we utilized these composition-adjustable Ag–Au SAMCs as SERS substrates to perform the trace detection of organic pollutants. As a powerful spectroscopy method, SERS has been widely applied in many fields, such as biology, chemistry, medicine, *etc.*[44–47] The remarkable SERS effects of noble metal nano/micro-structures can be attributed to the significant enhancement of LEMF at "hot-spots". Considering the tunable SPR frequency of the composition-adjustable Ag–Au SAMCs, their excellent SERS performance is expected. Firstly, the hollow porous structure of the Ag–Au SAMCs can serve as an ideal optical resonant cavity to harvest light and generate strong SPR coupling between the inner and outer surfaces of the shell, and hence generate strongly enhanced electric fields with large areas. Secondly, the high surface porosity not only endows the Ag–Au SAMCs with abundant inherent "hot-spots" for generating strong LEMF, but also provides huge surface area for the adsorption of probe molecules. Thirdly, the tunable SPR frequency enables the Ag–Au SAMCs to match well with the excitation wavelength, generating the strongest plasmon resonance. To investigate the programmable SERS performance of these Ag–Au SAMCs, we performed wavelength-dependent SERS measurements by employing various excitations, including 488, 514, 633, and 785 nm. Fig. 4a shows a typical control experiment using the as-synthesized 0.35 Ag–Au SAMC as a substrate to detect Rhodamine 6G (R6G) molecules (10^{-12} M) under different excitation wavelengths. It can be found that a strong background fluorescence arises in the spectrum under excitation of 514 nm wavelength, owing to the strong absorption of R6G at this wavelength. In order to avoid background fluorescence and improve the signal-to-noise ratio, we changed the excitation wavelength to 488, 633, and 785 nm. Comparing to the relatively weak enhancement under excitation wavelengths of 488 and 785 nm, the strongest SERS enhancement of 0.35 Ag–Au SAMCs can be obtained at an excitation wavelength of 633 nm, which is consistent with its strongest SPR absorption at this wavelength. The SERS intensity obtained under different excitation wavelengths matched well with its UV-vis absorption, as shown in Fig. 4b. These results demonstrated that utilizing the as-synthesized Ag–Au SAMCs can not only effectively avoid the fluorescence effect of probe molecules, but also enable us to programmably modulate the SPR frequency to match well with the illumination wavelength, obtaining the strongest SERS enhancement. Moreover, the SERS spectra of Rhodamine 6G

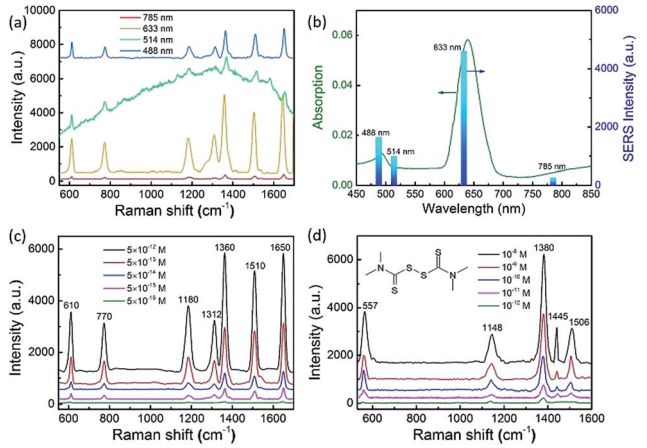

Fig. 4 (a) SERS spectra of R6G at a concentration of 10^{-12} M absorbed on 0.35 Ag–Au SAMCs at different excitation wavelengths of 488, 514, 633 and 785 nm respectively. (b) UV-vis spectra of 0.35 Ag–Au SAMCs and the SERS intensity of R6G (10^{-12} M) at 1650 cm^{-1} obtained from 0.35 Ag–Au SAMCs at different excitation wavelengths of 488, 514, 633 and 785 nm, respectively. SERS spectra of (c) R6G and (d) thiram in various concentrations obtained from the 0.35 Ag–Au SAMCs under excitation at 633 nm.

(R6G) with various concentrations in the range of 10^{-12} to 10^{-16} M are shown in Fig. 4c. It was seen that the peaks of R6G located at 1360 and 1650 cm^{-1} could still be clearly observed even at an ultralow concentration of 5×10^{-16} M. Based on the standard equation, the EF is calculated to be 1.3×10^{11} (see section S11 for details†), which is the highest value among the reported alloy microstructures (Table S2†). In addition, the as-synthesized Ag–Au SAMCs also display excellent spectral uniformity and reproducibility, which can be confirmed through comparing the SERS spectra collected from ten different test spots (Fig. S11†).

Based on the ultrahigh sensitivity of the Ag–Au SAMCs, they were further used as a chemosensor to perform the trace detection of thiram (tetramethylthiuram disulfide), which is a kind of contact fungicide widely used as a pesticide in agriculture. The breakdown of thiram releases carbon disulfide, which is seriously toxic to liver cells.[48,49] Due to its high toxicity, thiram has been classified as a highly hazardous to human health insecticide by the World Health Organization.[50] Thus developing a facile trace detection method for thiram residue in the environment is crucial. Fig. 4d shows the SERS spectra of thiram utilizing the 0.35 Ag–Au SAMCs under illumination at 633 nm. Well-resolved spectra of thiram with high signal-to-noise ratio can be clearly obtained based on these Ag–Au SAMCs. The peaks located at 557, 1148, 1380, 1445, and 1506 cm^{-1} are associated with the thiram molecules.[45] Significantly, the feature spectral peaks (1148 and 1380 cm^{-1}) can still be observed even down to an ultralow concentration of 10^{-12} M. Moreover, in addition to the high sensitivity, a promising chemosensor should possess excellent chemical stability. To investigate the chemical stability of the Ag–Au SAMCs, a control experiment was performed through recording the SERS spectra of thiram obtained from the 0.35 Ag–Au SAMCs before and after immersing in H_2O_2 solution. The results showed that compared to the poor chemical stability of pure Ag microcages in H_2O_2 solution, the 0.35 Ag–Au SAMCs still possessed excellent SERS activity even after immersion in 1% H_2O_2 solution for 5 h (Fig. S13†). The excellent oxidation resistance and chemical stability enable the Ag–Au SAMCs to act as a reliable chemosensor in an oxidative environment and meet the requirements of practical application.

Conclusions

In conclusion, we have demonstrated a facile strategy to realize tunable plasmon resonance based on composition-adjustable Ag–Au SAMCs with excellent shape-regularity and high uniformity. The SPR frequency of the Ag–Au SAMCs can be continuously and exquisitely modulated nearly without resonance deterioration when adjusting the composition ratio, which can be attributed to the perfect homogeneity of the elemental distribution on the atomic-level. The tunable SPR frequency endows the Ag–Au SAMCs with an ultrahigh EF of 1.3×10^{11} by adjusting the SPR frequency to be the same as the incidence wavelength, which is the highest value among reported alloy microstructures. As a typical demo, the as-synthesized 0.35 Au–Ag SAMCs can detect trace amounts of thiram at an ultralow concentration of 10^{-12} M. In addition to the ultrahigh sensitivity, the Au–Ag SAMCs also possess excellent chemical stability and meet stringent requirements in an oxidative environment. The progress made so far will guide future development in structure design and fabrication of high-performance SERS-based chemosensors, in addition fuelling the exploration of such a new class of Ag–Au SAMCs for practical applications in programmable SERS technology.

Experimental

Synthesis of Cu_2O octahedral templates

Cu_2O octahedrons were fabricated based on a previous report.[51] 4.5 g polyvinylpyrrolidone was dissolved in 100 mL 0.01 M $CuCl_2 \cdot 2H_2O$ aqueous solution. Then, 10.0 mL 2.0 M NaOH aqueous solution was added dropwise to the above solution. After stirring for 0.5 h, 10.0 mL 0.6 M ascorbic acid aqueous solution was further added dropwise to the mixed solution. The mixture was aged for 3 h. All of the procedure was carried out under constant stirring and heated to 55 °C in a water bath. The resulting precipitate was collected by centrifugation, and washed with deionized water and ethanol repeatedly to remove the residual inorganic ions and polymer, and finally dried under vacuum at 60 °C for 5 h for further characterization and use.

Synthesis of octahedral hollow Ag microcages and composition-adjustable Ag–Au substitutional alloy microcages (SAMCs)

Cu_2O templates (4.29 mg) were dispersed in 80 mL deionized water and 20 mL ethanol mixed solution by ultrasonic vibration for 10 min, then 1.2 mL sodium citrate aqueous solution (30 mM) and 1.05 mL $NaBH_4$ aqueous solution (100 mM) were

dropped sequentially into the solution containing the Cu_2O templates. After being stirred for 5 min, 1.05 mL $AgNO_3$ aqueous solution (10 mM) was added dropwise to the vigorously stirred mixture. The colour of the solution changes from orange to light yellow, indicating the formation of small Ag nanoparticles. As the reaction proceeded for 1 h, the solution gradually became dark yellow, indicating the formation of core–shell Cu_2O@Ag microstructures. Subsequently, 1.2 mL CH_3COOH aqueous solution (1 vol%) was injected into the above-mentioned mixture, the reaction lasted for another 2 h in order to completely dissolve the Cu_2O templates. The precipitate was collected by centrifugation, and re-dispersed in a mixed solution containing 80 mL deionized water and 20 mL ethanol. Then 1.2 mL sodium citrate aqueous solution (30 mM) and 100 μL $NaBH_4$ aqueous solution (100 mM) was added and the solution was stirred. Then 0–0.6 mL $HAuCl_4 \cdot 4H_2O$ aqueous solution (5.0 mM) was added dropwise to the above solution. The solution was stirred for a further 30 min, the resulting precipitate was collected by centrifugation and decanting, washed with distilled water and absolute ethanol several times, and then dispersed in absolute ethanol for further characterization. The products were Ag microcages, 0.1 Ag–Au SAMCs, 0.2 Ag–Au SAMCs, 0.3 Ag–Au SAMCs, 0.35 Ag–Au SAMCs, 0.4 Ag–Au SAMCs, 0.5 Ag–Au SAMCs, 0.6 Ag–Au SAMCs.

For SERS measurements

The as-prepared Ag–Au SAMCs were firstly dropped onto the cleaned silicon wafer (0.4×0.4 cm^2). Rhodamine 6G (R6G) and thiram were used as Raman probe molecules. Then, 100 μL of an ethanol aqueous Rhodamine 6G (R6G) or thiram solution was dripped onto the silicon wafer. After the samples were completely dried in air, the substrates were analyzed using a Raman spectrometer. The acquisition time was 10 s for each spectrum. For each sample, we obtained three SERS spectra at different positions on the substrate and then took the average values of them.

Conflicts of interest

There are no conflicts to declare.

Acknowledgements

This project is supported by the National Natural Science Foundation of China (No. 51272012, 21471013), the National Basic Research Program of China (2014CB931802) and Fundamental Research Funds for the Central Universities (ZG216S1797).

Notes and references

1 A. Tanaka, K. Hashimoto, B. Ohtani and H. Kominami, *Chem. Commun.*, 2013, **49**, 3419.
2 H. Eom, J.-Y. Jung, Y. Shin, S. Kim, J.-H. Choi, E. Lee, J.-H. Jeong and I. Park, *Nanoscale*, 2014, **6**, 226.
3 T. Wu, S. Liu, Y. Luo, W. Lu, L. Wang and X. Sun, *Nanoscale*, 2011, **3**, 2142.
4 Y. Xu, A. Cottenden and N. B. Jones, *Opt. Quantum Electron.*, 2005, **37**, 1129.
5 J. F. Li, Y. F. Huang, Y. Ding, Z. L. Yang, S. B. Li, X. S. Zhou, F. R. Fan, W. Zhang, Z. Y. Zhou, Y. WuDe, B. Ren, Z. L. Wang and Z. Q. Tian, *Nature*, 2010, **464**, 392.
6 M. Kang, J.-J. Kim, Y.-J. Oh, S.-G. Park and K.-H. Jeong, *Adv. Mater.*, 2014, **26**, 4510.
7 H. Im, K. C. Bantz, S. H. Lee, T. W. Johnson, C. L. Haynes and S.-H. Oh, *Adv. Mater.*, 2013, **25**, 2678.
8 H. Lee, J.-H. Lee, S. M. Jin, Y. D. Suh and J.-M. Nam, *Nano Lett.*, 2013, **13**, 6113.
9 A. Jakab, C. Rosman, Y. Khalavka, J. Becker, A. Trügler, U. Hohenester and C. Sönnichsen, *ACS Nano*, 2011, **5**, 6880–6885.
10 R. A. Hackler, M. O. McAnally, G. C. Schatz, P. C. Stair and R. P. Van Duyne, *J. Am. Chem. Soc.*, 2017, **139**, 2456.
11 R. Gunawidjaja, E. Kharlampieva, I. Choi and V. V. Tsukruk, *Small*, 2009, **5**, 2460.
12 A. Baba, N. Aoki, K. Shinbo, K. Kato and F. Kaneko, *ACS Appl. Mater. Interfaces*, 2011, **3**, 2080.
13 W. Huang, W. Qian and M. A. El-Sayed, *J. Am. Chem. Soc.*, 2006, **128**, 13330.
14 M. K. Gupta, S. Chang, S. Singamaneni, L. F. Drummy, R. Gunawidjaja, R. R. Naik and V. V. Tsukruk, *Small*, 2011, **7**, 1192.
15 P. K. Jain and M. A. El-Sayed, *Nano Lett.*, 2007, **7**, 2854.
16 Z. Fang, J. Cai, Z. Yan, P. Nordlander, N. J. Halas and X. Zhu, *Nano Lett.*, 2011, **11**, 4475.
17 M. A. Mahmoud, M. Chamanzar, A. Adibi and M. A. El-Sayed, *J. Am. Chem. Soc.*, 2012, **134**, 6434.
18 T. R. Jensen, M. L. Duval, K. L. Kelly, A. A. Lazarides, G. C. Schatz and R. P. Van Duyne, *J. Phys. Chem. B*, 1999, **103**, 9846.
19 M. A. Noginov, V. A. Podolskiy, G. Zhu, M. Mayy, M. Bahoura, J. A. Adegoke, B. A. Ritzo and K. Reynolds, *Opt. Express*, 2008, **16**, 1385.
20 I. Zorić, M. Zäch, B. Kasemo and C. Langhammer, *ACS Nano*, 2011, **5**, 2535.
21 Y. B. Zheng, J. L. Payton, C.-H. Chung, R. Liu, S. Cheunkar, B. K. Pathem, Y. Yang, L. Jensen and P. S. Weiss, *Nano Lett.*, 2011, **11**, 3447.
22 H. Shi, L. Zhang and W. Cai, *J. Appl. Phys.*, 2000, **87**, 1572–1574.
23 S. Link and M. A. El-Sayed, *J. Phys. Chem. B*, 1999, **103**, 4212.
24 P. Guo, D. Sikdar, X. Huang, K. J. Si, W. Xiong, S. Gong, L. W. Yap, M. Premaratne and W. Cheng, *Nanaoscale*, 2015, **7**, 2862.
25 W. Xiong, D. Sikdar, L. W. Yap, M. Premaratne, X. Lic and W. Cheng, *Nanaoscale*, 2015, **7**, 3445.
26 S. Liu, G. Chen, P. N. Prasad and M. T. Swihart, *Chem. Mater.*, 2011, **23**, 4098.
27 C. Wang, H. Yin, R. Chan, S. Peng, S. Dai and S. Sun, *Chem. Mater.*, 2009, **21**, 433.
28 C. Zhu, S. Guo and S. Dong, *Adv. Mater.*, 2012, **24**, 2326.

29 L. Bu, J. Ding, S. Guo, X. Zhang, D. Su, X. Zhu, J. Yao, J. Guo, G. Lu and X. Huang, *Adv. Mater.*, 2015, **27**, 7204.
30 Q. Zhang, J. Xie, J. Liang and J. Y. Lee, *Adv. Funct. Mater.*, 2009, **19**, 1387.
31 C. Gao, Y. Hu, M. Wang, M. Chi and Y. Yin, *J. Am. Chem. Soc.*, 2014, **136**, 7474.
32 S. E. Skrabalak, J. Chen, Y. Sun, X. Lu, L. Au, C. M. Cobley and Y. Xia, *Acc. Chem. Res.*, 2008, **41**, 1587.
33 Z. Liu, L. Cheng, L. Zhang, Z. Yang, Z. Liu and J. Fang, *Biomaterials*, 2014, **35**, 4099.
34 M. Gaudry, J. Lermé, E. Cottancin, M. Pellarin, J. L. Vialle, M. Broyer, B. Prével, M. Treilleux and P. Mélinon, *Phys. Rev. B*, 2001, **64**, 085407.
35 G. Guisbiers, R. Mendoza-Cruz, L. Bazán-Díaz, J. J. Velázquez-Salazar, R. Mendoza-Perez, J. A. Robledo-Torres, J.-L. Rodriguez-Lopez, J. M. Montejano-Carrizales, R. L. Whetten and M. José-Yacamán, *ACS Nano*, 2016, **10**, 188.
36 Y. Xiong, J. M. McLellan, J. Chen, Y. Yin, Z.-Y. Li and Y. Xia, *J. Am. Chem. Soc.*, 2005, **127**, 17118.
37 Y. Cao, R. Jin and C. A. Mirkin, *J. Am. Chem. Soc.*, 2001, **123**, 7961.
38 F. Huang, G. Ma, J. Liu, J. Lin, X. Wang and L. Guo, *Small*, 2016, **12**, 5442.
39 A. Coomar, C. Arntsen, K. A. Lopata, S. Pistinner and D. Neuhauser, *J. Chem. Phys.*, 2011, **135**, 084121.
40 U. Kreibig and M. Vollmer, *Optical Properties of Metal Clusters*, Springer, Berlin, New York, 1995.
41 J. R. Krenn, G. Schider, W. Rechberger, B. Lamprecht, A. Leitner, F. R. Aussenegg and J. C. Weeber, *Appl. Phys. Lett.*, 2000, **77**, 3379.
42 G. Mie, *Ann. Phys.*, 1908, **330**, 377.
43 E. Cottancin, J. Lermé, M. Gaudry, M. Pellarin, J. L. Vialle, M. Broyer, B. Prével, M. Treilleux and P. Mélinon, *Phys. Rev. B*, 2000, **62**, 5179.
44 L. Chen, L. Luo, Z. Chen, M. Zhang, J. A. Zapien, C. S. Lee and S. T. Lee, *J. Phys. Chem. C*, 2010, **114**, 93.
45 X. Qian, X.-H. Peng, D. O. Ansari, Q. Yin-Goen, G. Z. Chen, D. M. Shin, L. Yang, A. N. Young, M. D. Wang and S. Nie, *Nat. Biotechnol.*, 2008, **26**, 83.
46 P. Alonso-González, P. Albella, M. Schnell, J. Chen, F. Huth, A. García-Etxarri, F. Casanova, F. Golmar, L. Arzubiaga, L. E. Hueso, J. Aizpurua and R. Hillenbrand, *Nat. Commun.*, 2012, **3**, 684.
47 J. Lin, Y. Shang, X. Li, J. Yu, X. Wang and L. Guo, *Adv. Mater.*, 2017, **29**, 1604797.
48 P. Guo, D. Sikdar, X. Huang, K. J. Si, W. Xiong, S. Gong, L. W. Yap, M. Premaratne and W. Cheng, *Nanoscale*, 2015, **7**, 2862.
49 X. Zheng, Y. Chen, Y. Chen, N. Bi, H. Qi, M. Qin, D. Song, H. Zhang and Y. Tian, *J. Raman Spectrosc.*, 2012, **43**, 1374.
50 L. You, Q. An, J. Guo, J. Hu and C. Wang, *RSC Adv.*, 2013, **3**, 17469.
51 D. Zhang, H. Zhang, L. Guo, K. Zheng, X. Han and Z. Zhang, *J. Mater. Chem.*, 2009, **19**, 5220.